PROCEEDINGS A

rspa.royalsocietypublishing.org

Research

Article submitted to journal

Subject Areas:

xxxx

Keywords:

xxxx

Author for correspondence:

Insert corresponding author name

e-mail: pier.ledda@epfl.ch

Secondary instability in thin film flows under an inclined plane: growth of lenses on spatially-developing rivulets

Pier Giuseppe Ledda and François Gallaire

Laboratory of Fluid Mechanics and Instabilities, École Polytechnique Fédérale de Lausanne, Lausanne, CH-1015, Switzerland

The response of a thin film flowing under an inclined plane, modeled using the lubrication equation, is studied. The flow at the inlet is perturbed by the superimposition of a spanwise-periodic steady modulation and a decoupled temporally-periodic but spatially-homogeneous perturbation. As the consequence of the spanwise inlet forcing, so-called rivulets grow downstream and eventually reach a streamwise-invariant state, modulated along the direction perpendicular to the flow. The linearized dynamics in the presence of a time-harmonic inlet forcing shows the emergence of a time-periodic flow characterized by drop-like structures (so-called lenses) that travel on the rivulet. The spatial evolution is rationalized by a weakly non-parallel stability analysis. The occurrence of the lenses, their spacing and thickness profile, is controlled by the inclination angle, flow rate, and the frequency and amplitude of the time-harmonic inlet forcing. The faithfulness of the linear analyses is verified by non-linear simulations. The results of the linear simulations with inlet forcing are combined with the computations of non-linear traveling lenses solutions in a double-periodic domain to obtain an estimate of the dripping length, for a large range of conditions.

Author Accepted Manuscript of:

Ledda Pier Giuseppe and Gallaire François. 2021 Secondary instability in thin film flows under an inclined plane: growth of lenses on spatially developing rivuletsProc. R. Soc. A.47720210291 - http://doi.org/10.1098/rspa.2021.0291

© 2021 The Author(s). Published by the Royal Society. All rights reserved.

© The Authors. Published by the Royal Society under the terms of the Creative Commons Attribution License http://creativecommons.org/licenses/by/4.0/, which permits unrestricted use, provided the original author and source are credited.

THE ROYAL SOCIETY PUBLISHING

1. Introduction

The study of the dynamics of coating flows is of undeniable interest owing to its wide presence in natural environments [1–5] and the large number of applications in industrial and manufacturing processes [6,7]. Exhibiting a broad variety of flow behaviors, first systematic analyses of coating flows were performed in the pioneering works of P.L. Kapitza and S.P. Kapitza, in inertia-driven flows [8–10]. Besides, intriguing patterns in coating flows may emerge due to other physical mechanisms as Marangoni effects [11–14], contact-line driven instabilities [15–18], or the Rayleigh-Taylor instability [19].

According to the pioneering studies of Rayleigh [20] and Taylor [21], when a heavier fluid lies above a lighter fluid, a flat interface is unstable to perturbations. When only gravity is considered, all wavelengths are unstable. The range of unstable wavelengths is bounded when capillary effects are considered [22]. The Rayleigh-Taylor instability of a thin film lying below a horizontal substrate (whose normal points to the opposite direction of the gravity vector) has been widely studied in the literature, starting from the work of Hynes [23]. In a situation in which the film thickness is sufficiently small compared to the characteristic deformation lengths along the horizontal directions, the lubrication approximation can be employed [24]. The instability leads to pendent drops [25]. The equilibrium of such pendent drops was theoretically studied by Pitts [26], demonstrating the existence of a critical volume beyond which the pendent drop is unstable, as also shown in Marthelot et al. [27]. For sufficiently large thicknesses, these pendent drops algebraically grow and drip [28]. The experimental investigation of Fermigier et al. [29] showed that such pendent drops organize in hexagonal or square patterns.

When the substrate is tilted, the gravity component parallel to the substrate drives a flow and a variety of patterns and dynamics were observed. Brun et al. [30] investigated the dripping threshold relating it to the absolute instability of the flat film configuration. However, further investigations in Scheid et al. [31] and Kofman et al. [32] showed that the absolute regime does not predict the dripping satisfactorily. A further numerical study by Rohlfs et al. [33] showed the existence of stationary traveling waves, invariant along the direction perpendicular to the flow.

Charogiannis et al. [34] performed an experimental campaign with a permanent influx, identifying several three-dimensional patterns ranging from structures purely modulated along the direction perpendicular to the flow (*spanwise* direction), so-called *rivulets* (see sketch of figure 1), to more complicated configurations with rivulets carrying traveling lenses. These rivulet patterns were reminiscent of those observed in Lerisson et al. [35] in a similar set-up, and by Rietz et al. [36], for a thin film on the outside of a vertical rotating cylinder.

Lerisson et al. [37] compared experiments with theoretical and numerical findings, showing that, for some conditions of inclination angle and flow rate, a steady pattern of rivulets was reached. After some distance from the inlet, these rivulets were characterized by a central lobe of very large thickness and side lobes of very small thickness. The authors showed that the central lobe was a streamwise-invariant profile well described by a two-dimensional pendent drop shape, similar to the results of Pitts [38], but with a flow rate constraint rather than a volume one. Subsequently, in Ledda et al. [39], the authors performed a secondary stability analysis of these streamwise-saturated states, highlighting a strong stabilization mechanism as the plate was inclined or the flow rate reduced. For small inclinations and large flow rates, traveling lenses grew on the rivulets (see figure 1(a)), whose initial growth was well described by the linear stability analysis. The non-linear behavior of such lenses was studied by Indeikina et al. [40], where the authors experimentally investigated the dripping from a rivulet and described the traveling lenses solution by matched asymptotic expansions, using a lubrication equation with the linearized expression of the curvature. They interpreted the blow-up of the numerical solution of the lubrication equation as the initial stage of dripping.

In Lerisson et al. [35], for a certain range of flow rate and inclination angle, the occurrence and the spacing of these traveling lenses were experimentally tuned using a harmonic forcing at the inlet, consisting of a variation of the total flow rate injected below the substrate. As confirmed by

Ledda et al. [39], the streamwise-invariant rivulet profiles behaved as noise amplifiers in a certain region of the parameter space. In such conditions, the flow instability depends on the imposed temporal forcing at the inlet [41–44].

The study of pattern formation in complex flows relies on several theoretical approaches to shed light on the resulting structures [19]. Among these methodologies, in this work we focus on linear and non-linear analyses, which are in turn classified in local, weakly non-parallel, and global approaches. Linear analyses stem from the linearization of the flow equations under the assumption of small perturbations with respect to the so-called baseflow [45–47]. In this work, the base flow evolves along the streamwise direction, i.e. it is non-parallel, and it is obtained through steady non-linear numerical simulations described in Section 3. When the baseflow is steady, the perturbation is expanded in normal form in time, i.e. $\sim \exp[\lambda t]$, and the linear stability analysis is called global [47]. If the baseflow is invariant along one direction x_1, the perturbation can be expanded in normal form also along x_1 (local stability analysis) [45,46]. An intermediate situation occurs when the base flow slowly evolves along this direction. The separation of scales between the evolution of the baseflow and the perturbation allows one to perform a weakly non-parallel (WKBJ) stability analysis [45,48,49]. The local stability analysis problems at each x_1 section are solved and then smoothly reconnected via an amplitude equation. In all these linear problems, one typically obtains eigenfunction or linear forced problems, with computational times significantly lower compared to the non-linear analyses, making them suitable for parametric studies. The predictions often include the most unstable wavelength and frequency of the instability from the local stability analysis [19] or the global structure of the unstable mode [46,47]. Weakly non-parallel approaches are less computationally expensive than global analyses and give further detail about the nature of the global instability and an accurate description of the global mode. Non-linear analyses are complementary to the linear ones to verify their faithfulness and investigate phenomena at larger amplitudes of the perturbation, where the linear analyses cease to be valid. We will perform streamwise periodic non-linear simulations to describe dripping lenses riding on a saturated rivulet profile in Section 6 as well as fully non-linear global numerical simulations in Sections 5 and 7.

In this work, the complex interface patterns governing the thin film dynamics, with the development of growing lenses on the top of spatially developing rivulets, are investigated by focusing on the secondary instability of one single and spanwise-periodic rivulet, with a perspective on the dripping phenomenon. The paper is organized as follows. In Section 2 the lubrication model and the numerical implementation are presented. Subsequently, Section 3 is devoted to the analysis of the steady rivulet emerging when a slightly modulated constant thickness is imposed at the inlet, which will serve as a base state for the secondary stability analysis conducted in Section 4, where the linearized dynamics of lenses around the steady baseflow solution when the inlet is forced via a harmonic forcing is studied. In Section 4(c), the observed patterns are rationalized via a weakly non-parallel (WKBJ) local stability analysis. Subsequently, the non-linear response to harmonic inlet forcing is studied, and eventually the non-linear periodic traveling lens solutions in periodic domains of various lengths is investigated. This allows us, in Section 7, to unify the results of the previous sections to give an estimate of the dripping length for a large range of inclination angle and flow rate.

2. Governing equation and numerical method

In this section, the governing equation for a thin film coating the underside of an inclined plane and its numerical implementation are introduced. We consider a thin film of thickness $\hat{h}$, of a viscous fluid flowing under a planar substrate, inclined with respect to the vertical direction of an angle θ. The streamwise and spanwise directions are denoted $(\hat{x}, \hat{y})$ (see figure 1). The streamwise component of the gravity g reads $g_x = g\cos(\theta)$, while there is no projection along the spanwise direction. The fluid properties are the viscosity μ, the density ρ, and the surface tension coefficient γ. The capillary length $\ell_c = \sqrt{\gamma/(\rho g)}$ and the characteristic film thickness h_N are introduced. The

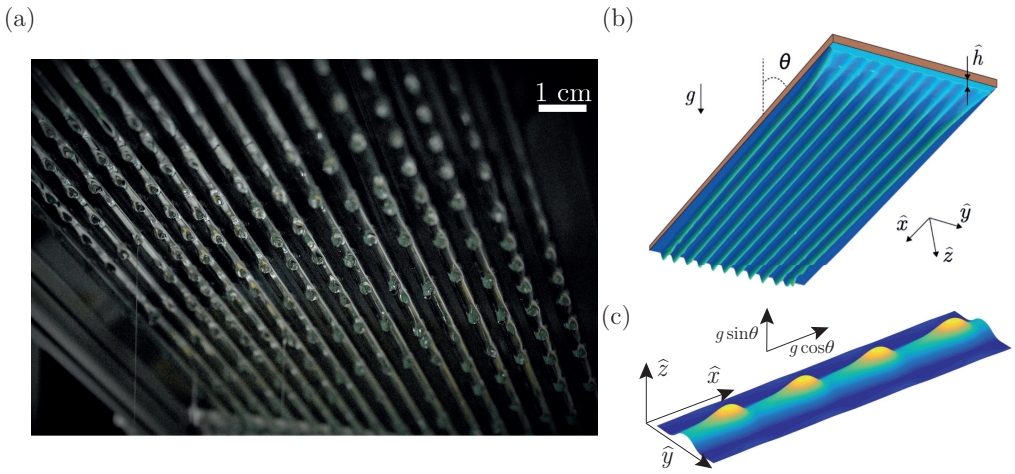

Figure 1: (a) Experimental photo of rivulets that carry lenses below an inclined planar substrate. The fluid is silicon oil, of viscosity $\mu \approx 1\,\mathrm{Pa\,s}$ and density $\rho \approx 970\,\mathrm{kg/m^3}$. The inclination angle with respect to the vertical is 45° and the film thickness is $\approx 1\,\mathrm{mm}$. (b) Sketch of the flow configuration, with rivulets that invade the domain and lenses of small amplitude observed downstream. (c) Sketch of a single rivulet that is carrying lenses.

characteristic time scale of the Rayleigh-Taylor instability reads

$$\tau = \frac{\nu \ell_c^2}{h_N^3 g \sin^2\theta}. \tag{2.1}$$

Spatial directions $\hat{x}$ and $\hat{y}$ are non-dimensionalized by the reduced capillary length $\ell_c^* = \ell_c/\sqrt{\sin\theta}$, thickness $\hat{h}$ by h_N and time by τ:

$$x = \hat{x}/\ell_c^*, \quad y = \hat{y}/\ell_c^*, \quad h = \hat{h}/h_N, \quad t = \hat{t}/\tau. \tag{2.2}$$

The modelization of the flow of a thin film is based on the separation of scales between the normal and tangential to the substrate length scales [10]. Different levels of approximation are employed to describe the flow, depending on the considered regime. A set of boundary layer equations holds for thin film flows mostly governed by gravity and surface tension [50]. When the inertia of the flow is small, the boundary layer equations are further simplified, leading to a single evolution equation for the thickness, called Benney equation [51–53]. Pumir et al. [54] numerically observed a blow-up of the solution at large Reynolds numbers. To further extend these models at larger Reynolds numbers, more refined methods have been proposed [31,55]. However, in this work we consider the situation in which the Reynolds number is very small and inertial effects can be neglected. Despite this assumption, a plethora of patterns is observed, since these simple non-inertial models already incur complex non-linearities [35,37]. For negligible inertia, the Benney equation is accurate and widely employed [52]. The thin film model with the complete expression of the curvature κ [6,37,39,56–58] is thus considered, together with the above-defined non-dimensionalization:

$$\frac{\partial h}{\partial t} + \tilde{\ell}_c^* \cot(\theta) h^2 \frac{\partial h}{\partial x} + \frac{1}{3}\nabla \cdot (h^3(\nabla h + \nabla \kappa)) = 0, \tag{2.3}$$

where ∇ operates in the (x, y) plane, $\tilde{\ell}_c^* = \ell_c^*/h_N$ and κ is the mean curvature:

$$\kappa = \frac{\frac{\partial^2 h}{\partial x^2}\left(1+\left(\frac{1}{\tilde{\ell}_c^*}\frac{\partial h}{\partial y}\right)^2\right) + \frac{\partial^2 h}{\partial y^2}\left(1+\left(\frac{1}{\tilde{\ell}_c^*}\frac{\partial h}{\partial x}\right)^2\right) - 2\left(\frac{1}{\tilde{\ell}_c^*}\right)^2 \frac{\partial h}{\partial x}\frac{\partial h}{\partial y}\frac{\partial^2 h}{\partial x \partial y}}{\left(1+\left(\frac{1}{\tilde{\ell}_c^*}\frac{\partial h}{\partial x}\right)^2 + \left(\frac{1}{\tilde{\ell}_c^*}\frac{\partial h}{\partial y}\right)^2\right)^{3/2}}. \tag{2.4}$$

The linear advection velocity $u = \tilde{\ell}_c^* \cot(\theta)$ is introduced, which is the velocity of advection of thickness perturbations of a flat film [30]. Note that the reported non-dimensionalized curvature differs from Lerisson et al. [37], where the presence of the terms $1/\tilde{\ell}_c^*$ was overlooked and assumed to be unitary. In this work, we perform our analytical and numerical analyses for the case $\tilde{\ell}_c^* = 1$ and study the effect of u. This choice stems from our aim to put a maximum emphasis on the non-linear curvature effects, which ensure an unstable behavior of the flow in a large range of u.

A configuration in which the flow is continuously fed at the inlet is considered. Spanwise-periodic rivulet structures emerge and invade the domain, with a natural spacing $L_y = 2\pi\sqrt{2}$ [37]. In this work, we numerically investigate the evolution of one spanwise-periodic rivulet, of natural spanwise periodicity L_y, when the inlet is temporally forced. A rectangular domain of streamwise length L_x and spanwise length $L_y = 2\pi\sqrt{2}$ is considered, with inlet and outlet conditions along the streamwise direction and periodic boundary conditions imposed along the spanwise direction. The inlet condition is a flat film perturbed by a cosine along the spanwise direction (of amplitude A and wavelength L_y) and by a time-periodic forcing $\tilde{f}$ (of amplitude ε), imposed by a Dirichlet boundary condition of the form:

$$h(x = 0, y) = 1 + \mathrm{A}\cos(y/\sqrt{2}) + \varepsilon \tilde{f}(y, t). \tag{2.5}$$

The outlet condition is imposed by employing a Sponge method, as in Lerisson et al. [37], resulting in the following equation to be numerically solved in the whole domain:

$$\frac{\partial h}{\partial t} + \tilde{\ell}_c^* \cot(\theta) h^2 \frac{\partial h}{\partial x} + \frac{1}{3}\nabla \cdot (h^3(\nabla h + \nabla \kappa)) = \mathrm{Sp}(x)(h - 1), \tag{2.6}$$

where $\mathrm{Sp}(x) = -\frac{1}{2}(1 + \tanh(x - 6L_x/7))$ is the Mask function of the Sponge method [59] that ensures the relaxation of the thickness to $h = 1$ and avoids reflections from the outlet.

Equations (2.4,2.6) are numerically implemented in the finite-element solver COMSOL Multiphysics, employing third-order Lagrange shape functions. Both the steady and unsteady solver are employed, exploiting respectively the built-in Newton-Rapson algorithm and a second-order Backward Differentiation Formula. The Newton algorithm is initialized using the large-time solution ($t = 1000$) of the unsteady equation for a value of $u = 5$, in which no unsteady instabilities are numerically and experimentally observed owing to the large value of u [39]. The previous solution is taken as initial guess for successive and smaller values of u. In the following, the Sponge region is excluded from the results, leading to a domain of effective length $L_x = 225$, unless stated differently. Numerical convergence is achieved with a characteristic size of the elements equal to half of the reduced capillary length, already validated in previous works [37,39]. Furthermore, the presented results are not influenced by the imposed spanwise periodic length, both for the steady and unsteady simulations. In Appendix A of the Electronic Supplementary Material (ESM) some calculations for a spanwise size of $L_y = 4\pi\sqrt{2}$ and $L_y = 8\pi\sqrt{2}$ are repeated, which exclude the presence of steady and unsteady sub-harmonic instabilities for the considered spanwise wavelength forced at the inlet [45].

3. The steady baseflow

The present section is devoted to the study of the steady solution $h = H(x, y)$ of the flow equation (2.6), $\varepsilon = 0$, when inlet and outlet conditions in a spanwise-periodic box of span L_y are considered. In equation (2.5), $A = A^* = 10^{-2}$ is assumed. In figure 2 the thickness profile in the (x, y) plane, for decreasing values of u, is reported. In all cases, the thickness profile evolves from a flat condition

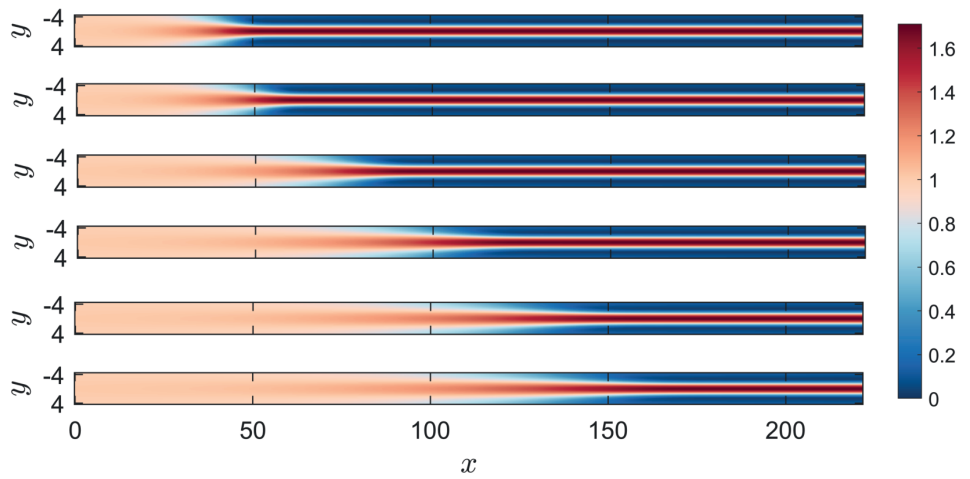

Figure 2: Two-dimensional visualization of the steady baseflow $H(x, y)$. From the top to the bottom: $u = 0.85$, $u = 1$, $u = 1.5$, $u = 2$, $u = 2.5$, $u = 2.75$.

at the inlet, slightly perturbed with a cosine, to a streamwise-invariant rivulet state. The more u decreases, the further downstream the streamwise-invariant rivulet state emerges.

In figure 2, (a) the variation of the minimum and maximum thickness with x (solid lines) and (b) the resulting spanwise profiles at different streamwise locations are reported. In panel (a), the maximum and the minimum thickness saturate respectively to $\sim 10^{-2}$ and ≈ 1.71. The presence of a streamwise saturation allows one to define a *healing* length L_h for the saturated rivulet profile, defined as the streamwise location beyond which $\frac{\mathrm{d}}{\mathrm{d}x} \max(H) < 10^{-4}$, marked by an asterisk in figure 3(a). The healing length always increases with u and has a linear dependence for $u > 0.75$. In panel (a), the dashed line denotes the streamwise amplification predicted by the steady dispersion relation of the flat film [37], briefly summarized as follows. Introducing in equation (2.3) the ansatz $h = 1 + \varepsilon\eta$, $\varepsilon \ll 1$, with $\eta \propto \exp(\mathrm{i}(k_x x + k_y y)$, the equation at $\mathcal{O}(\varepsilon)$ leads to the following dispersion relation:

$$\left(k_y^2 - k_y^4\right) + \left(k_x^4 + k_x^2 + 2k_x^2 k_y^2\right) = 3iuk_x, \tag{3.1}$$

where k_x and k_y are respectively the streamwise and spanwise wavenumbers. The estimated amplification then reads $\max_y(H) = 1 + \mathrm{A}\exp(\kappa x)$, where $\kappa = -\min(\mathrm{Im}(k_x))$ is the spatial growth rate (i.e. the opposite of the imaginary part of k_x) in the steady dispersion relation (3.1) (figure 12(a) of Lerisson et al. [37]), for $k_y = 1/\sqrt{2}$. The linear rivulet amplification well approximates the non-linear simulations results, for small values of the perturbation $\eta = H - 1$. The rivulet profiles (panel (b)) evolves from a slightly perturbed cosine to the saturated rivulet profile.

So far, the steady solution of the flow equation (2.3) was studied for $A = A^*$. Owing to the good agreement between the non-linear simulation and the linear rivulet amplification for low amplitudes $\max_y(H) - 1 \lessapprox 0.2$, these results are generalized to different values of A. When the amplitude is smaller than the studied case, i.e. $A < A^*$, the resulting mode is analogous to a cosine and the initial part is thus approximated as

$$H(x, y) = 1 + \mathrm{A}\exp(\kappa x)\cos(\frac{y}{\sqrt{2}}), \tag{3.2}$$

which is then connected, at some coordinate $x = x^* = \frac{1}{\kappa}\log\left(\frac{A^*}{A}\right)$, to the solution for $A = A^*$ reported in figure 2. In contrast, for $A^* < A < 0.2$, the solution is assumed to start at the coordinate

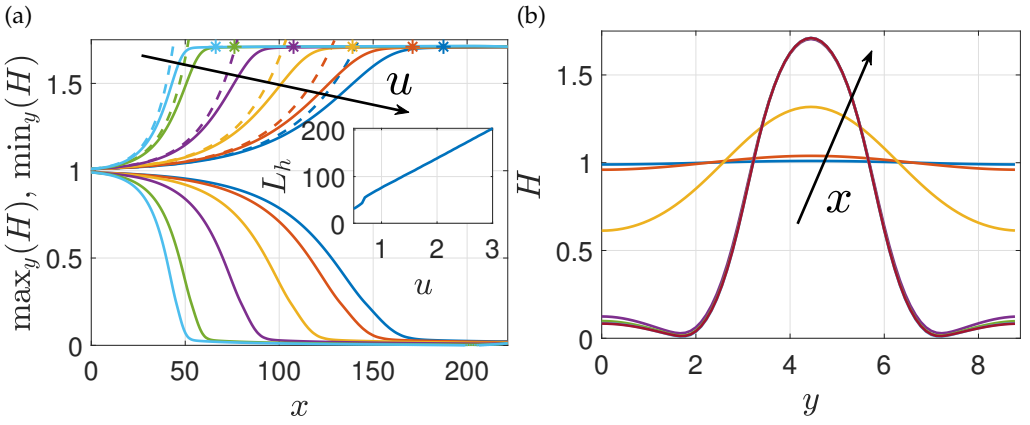

Figure 3: (a) Evolution with x of the maximum and minimum values of the steady baseflow $H(x,y)$, for $u=0.85$ (cyan), $u=1$ (green), $u=1.5$ (purple), $u=2$ (yellow), $u=2.5$ (orange), $u=2.75$ (blue). The stars denote the healing length for each value of u. In the inset: healing length as a function of u. (b) $u=2$. Evolution of the profile at different streamwise locations $x=0$ (blue), $x=25$ (orange), $x=50$ (yellow), $x=100$ (purple), $x=150$ (green), $x=200$ (cyan), $x=220$ (maroon).

$x=x_0$, where the reference solution $H(x,y)$ initiated with A^* attains A, i.e. $H(x_0,0)=A$. It thus consists of a variation of the origin of the x axis.

The steady simulations of equation (2.3) show that the rivulet evolves along the streamwise direction reaching a streamwise-saturated state. The latter is independent of u and is characterized by a central lobe of large thickness and side lobes of low thickness. While in the work of Ledda et al. [39] the attention was focused on the analysis of the evolution of unsteady perturbations of the streamwise-invariant rivulet profile, hereafter the streamwise evolution of the base flow starting at the inlet is included by studying the evolution of unsteady perturbations with respect to the two-dimensional steady baseflow $H(x,y)$.

4. Secondary stability analysis: linear response to harmonic inlet forcing

(a) Linearized dynamics around the baseflow solution

In this section, the equation describing the linearized dynamics of a thickness perturbation with respect to the steady baseflow $H(x,y)$ defined in the previous section is introduced. The following decomposition is considered:

$$h(x,y,t)=H(x,y)+\varepsilon\tilde{\eta}(x,y,t), \quad \varepsilon\ll 1, \tag{4.1}$$

where $\tilde{\eta}$ is the *perturbation* with respect to the baseflow $H(x,y)$. The decomposition (4.1) is next introduced in the flow equation (2.6), leading to the baseflow equation at leading order (i.e. the steady version of equation (2.3)) and the following equation at order ε:

$$\partial_t\tilde{\eta}+\frac{1}{3}\nabla\cdot\left(H^3\left(\nabla\tilde{\eta}+\nabla\tilde{\kappa}_{(1)}\right)+3H^2\left(\nabla H+\nabla\kappa_{(0)}+u\right)\tilde{\eta}\right)=\mathrm{Sp}(x)\tilde{\eta} \tag{4.2}$$

where the baseflow curvature $\kappa_{(0)}$ is given by equation (2.4) with $\tilde{\ell}_c^*=1$, while the first order $\tilde{\kappa}_{(1)}$ curvatures is expressed in terms of the x and y components of the normal vector at order ε and

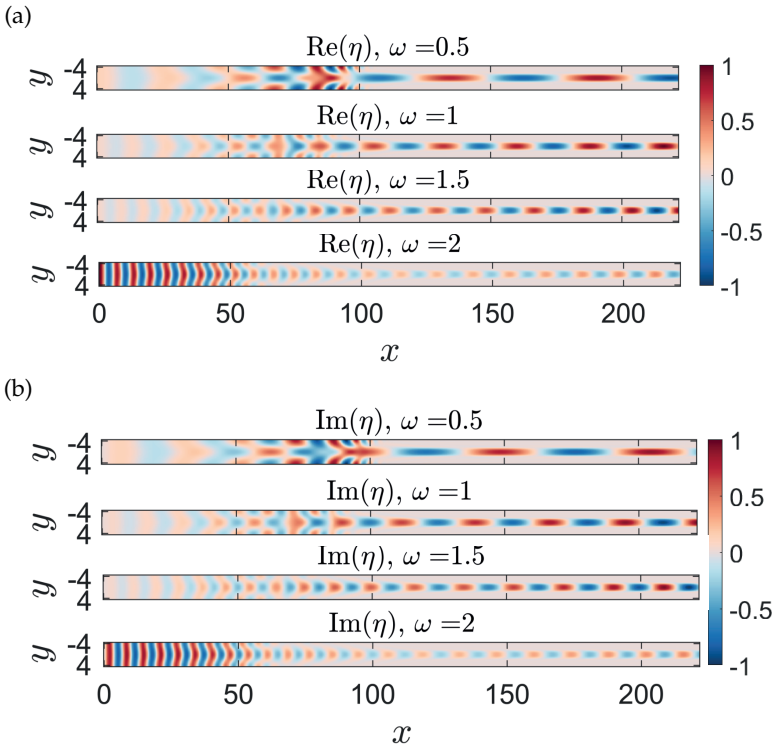

Figure 4: Global linear response, (a) real and (b) imaginary parts. Quantities are rescaled with the maximum absolute value, $u = 2$.

reads, upon assumption of $\tilde{\ell}_c^* = 1$:

$$\tilde{\kappa}_{(1)} = \nabla \cdot \tilde{\mathbf{n}}_{(1)}, \quad \tilde{\mathbf{n}}_{(1)} = \frac{[\partial_x \tilde{\eta}(1+\partial_y H^2) - \partial_y H \partial_y \tilde{\eta} \partial_x H, \partial_y \tilde{\eta}(1+\partial_x H^2) - \partial_y H \partial_x \tilde{\eta} \partial_x H]}{(1+\partial_x H^2 + \partial_y H^2)^{3/2}}, \quad (4.3)$$

and the inlet condition now reads:

$$\tilde{\eta} = \tilde{f}(y) = f(y)\exp(\mathrm{i}\omega t) \quad (4.4)$$

In analogy to the non-linear equation (2.6), the numerical implementation of (4.2) is performed in COMSOL Multiphysics.

The linearized equation (4.2) is the starting point for our analysis. In the following, the dynamics of thickness perturbations with respect to the steady baseflow $H(x, y)$, when the inlet is temporally forced via a harmonic forcing, is studied. As it is well known from the literature, the linear response of the base state for an external harmonic forcing is only well defined if the baseflow is globally stable with respect to perturbations, i.e. there is no intrinsic oscillatory behavior of the flow [44,45]. In Appendix B of the ESM, the global stability analysis is reported, revealing that the instability occurs for $u < u_0$, $u_0 = 0.56$. In the following, values of u larger than the global instability threshold, i.e. $u > u_0$, are considered, thus focusing on the regime in which the flow is said to be convectively unstable and behaves as a noise amplifier.

(b) Global linear analysis

In this section, we study the secondary instability of the spatially-developing and steady baseflow $H(x, y)$ subject to a harmonic inlet forcing $\tilde{f}$ of frequency ω, i.e. $\tilde{f} = f(y)\exp(\mathrm{i}\omega t)$. The equation for the linearized dynamics (4.2) together with the following ansatz for the perturbation $\tilde{\eta}$ are

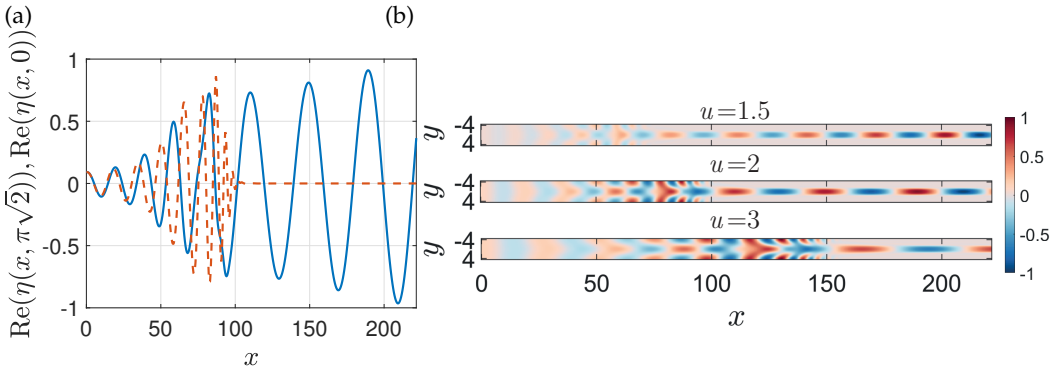

Figure 5: Real part of the global linear response, for $\omega = 0.7$, (a) at the centerline (solid) and on the lateral boundary (dashed), for $u = 2$, and (b) from the top to the bottom, $u = 1.5$, $u = 2$, $u = 3$.

considered:

$$\tilde{\eta}(x, y, t) = \eta(x, y) \exp(\mathrm{i}\omega t) \tag{4.5}$$

Substituting this expression in equation (4.2) and simplifying the exponential term, one obtains:

$$\mathrm{i}\omega\eta + \frac{1}{3}\nabla \cdot \left(H^3 \left(\nabla\eta + \nabla\kappa_{(1)} \right) + 3H^2 \left(\nabla H + \nabla\kappa_{(0)} + u \right) \eta \right) = \mathrm{Sp}(x)\eta, \tag{4.6}$$

with the Dirichlet boundary condition $\eta(x = 0, y) = f(y)$ at the inlet. The inlet forcing is first given by

$$f(y) = \frac{1}{\sqrt{L_y}}, \tag{4.7}$$

so that $\int_{\Gamma_i} |f|^2 \mathrm{d}y = 1$. This forcing can be experimentally reproduced, as it consists of a time-harmonic variation of the flow rate at the inlet, thus making this numerical study suitable for further experimental validations.

Equation (4.6), together with the boundary condition (4.7) at the inlet and periodic ones on the lateral sides, is a linear problem of the form $\mathrm{i}\omega\mathbf{I}\eta + \mathbf{L}\eta = \mathbf{B}f$, where $\mathbf{L}$ and $\mathbf{B}$ are respectively the linearized operator and the so-called prolongation operator, which maps the boundary forcing inside the domain. The numerical implementation is performed in COMSOL Multiphysics, in analogy to the baseflow computation.

Figure 4 shows the response η, for $u = 2$ and for different values of the forcing frequency ω. Close to the inlet, the perturbation strongly resembles a wavy oscillation, without any appreciable dependence on the y direction. In the streamwise-invariant rivulet region, drop-like structures, so-called *lenses*, are observed. The streamwise wavelength of the lenses decreases as ω increases. Coincidently, the transition region between wavy oscillations and lenses is moved slightly upstream. In this region, an intricate pattern is observed, with strong perturbations on the lateral sides that are then damped downstream. Concerning the streamwise amplification of the perturbation, a variety of behaviors is observed. For $\omega = 0.5$, the peak in the amplitude is located at $x \approx 100$, while for $\omega = 1$ and $\omega = 1.5$ it moves to the outlet. For $\omega = 2$, a strong damping of the so far growing oscillations is observed for $x > 50$, followed by a progressive and modest increase of the amplitude of the lenses.

In figure 5(a), the evolution of the real part of the perturbation at the centerline, i.e. $y = 0$, (solid line) and on the lateral side, i.e. $y = \pi\sqrt{2}$, (dashed line) is reported, for $\omega = 0.7$ and $u = 2$. Interestingly, at $x \approx 75$, close to the healing length L_h, the streamwise oscillations are not purely sinusoidal as they become further downstream, but a more intricate profile is observed, both at the centerline and on the lateral side.

Figure 5(b) presents the pattern for fixed forcing frequency $\omega = 0.7$ and for three different values of u. As u increases, the transition region is shifted downstream and lenses with increasing streamwise extension are observed.

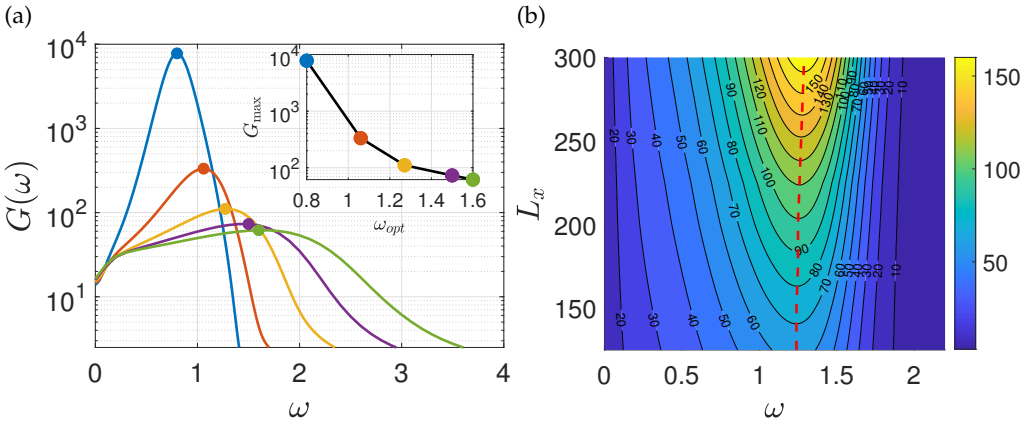

Figure 6: (a) Variation of the Gain $G(\omega)$ with ω and for $u = 1$ (blue), $u = 1.5$ (orange), $u = 2$ (yellow), $u = 2.5$ (purple), $u = 3$ (green). In the inset: maximum value and optimal frequency for different values of u. (b) Iso-contours of the Gain as a function of ω and the streamwise length of the domain L_x, $u = 2$.

We now turn to a quantitative analysis of the linear response. A long-established way of measuring the amplification of the response for a forcing frequency ω is the gain $G(\omega)$, defined as the ratio between the amplitude of the output response and the amplitude of the input forcing [44,45,60]. The gain is defined as follows:

$$G^2(\omega) = \frac{\int_\Omega |\eta|^2 \mathrm{d}x\mathrm{d}y}{\int_{\Gamma_i} |f|^2 \mathrm{d}y}, \tag{4.8}$$

where Ω denotes the whole domain and Γ_i the inlet boundary. Note that, according to the definition of f given in equation (4.7), the denominator of equation (4.8) is equal to one.

In figure 6(a) the gain $G(\omega)$, for different values of u, is reported. The gain curves are characterized by a maximum (*optimal*) value, associated with an optimal frequency. The optimal gain and frequency respectively increase and decrease as u decreases. From $u = 3$ to $u = 1$, the gain increases of two orders of magnitude, from 10^2 to 10^4, and the optimal frequency decreases from $\omega_{\mathrm{opt}} = 1.6$ to $\omega_{\mathrm{opt}} = 0.8$.

Since in some cases the maximum response is attained at the outlet, the effect of the streamwise length L_x of the domain on the gain is reported in figure 6(b), for $u = 2$. For a fixed frequency ω, the gain increases with the streamwise length. However, the optimal frequency only slightly varies with the streamwise length, from a value of $\omega_{\mathrm{opt}} = 1.24$ for $L_x = 125$ to $\omega_{\mathrm{opt}} = 1.29$ for $L_x = 300$.

The analysis of the linear response shows that, in the presence of a harmonic inlet forcing, a secondary instability occurs on the spatially-developing rivulet and perturbations evolve downstream into traveling lenses. The occurrence of such lenses is controlled by different parameters. The first one is the linear advection velocity u, which is a combination of inclination angle and flow rate. An increase of u leads to lenses of larger spacing and smaller amplitude. The harmonic inlet forcing frequency ω modifies both the spacing and the amplitude of the lenses.

An optimal frequency that most amplifies the lenses is identified. The weak dependence of the optimal frequency with the streamwise length of the domain indicates that the transition region from flat film to saturated rivulet is crucial for the evolution and amplification of the inlet forcing.

Finally, figures 4 and 5(a) show an intricate evolution of the oscillations, in particular close to the transition region between wavy oscillations and lenses. This observation suggests that there may be different spatial modes that interact as the perturbation is advected downstream.

In the following, the structure of the linear response is investigated by a weakly non-parallel local stability analysis.

(c) Weakly non-parallel stability analysis (WKBJ)

In a parallel convectively unstable flow, the spatial stability branches fully describe the response to harmonic forcing of frequency ω [49]. Within this framework, the perturbation with respect to the streamwise-invariant baseflow reads $\tilde{\eta} \propto \exp\left(\mathrm{i}\left(k_x x - \omega t\right)\right)$, where k_x is the complex streamwise wavenumber, resulting from the polynomial eigenvalue problem associated with the dispersion relation [45]. The imaginary and real parts of k_x respectively describe the amplification in space and the spatial frequency.

The weak non-parallelism of the baseflow $H(x,y)$ is included by employing the WKBJ formalism introduced by Gaster et al. [48]. A fast and slow streamwise scales are introduced, respectively denoted as x and $X = \sigma x$, where σ is a measure of the weak non-parallelism of the baseflow. The following ansatz for the perturbation $\tilde{\eta}$ is considered:

$$\tilde{\eta}(x,t) = \mathcal{A}(X)\eta(X,y)\exp\left[\mathrm{i}\left(\frac{1}{\sigma}\int_0^X k_x\left(X'\right)\mathrm{d}X' - \omega t\right)\right] \tag{4.9}$$

where η is the local eigenvalue and $\mathcal{A}(X)$ is the envelope function which smoothly connects the progressive slices of the spatial stability analysis. An asymptotic expansion in σ is performed on the linearized equation (4.2). The detailed derivation is reported in Appendix C of the ESM. At order $\mathcal{O}(1)$ the following eigenfunction problem is obtained:

$$-\mathrm{i}\omega\eta + (\mathrm{i}k_x)uH^2\eta + \frac{1}{3}\frac{\mathrm{d}}{\mathrm{d}y}[3H^2(\partial_y H + \partial_y\kappa_{(0)})\eta + \\ + H^3(\frac{\mathrm{d}\kappa_{(1)}}{\mathrm{d}y} + \frac{\mathrm{d}\eta}{\mathrm{d}y})] - \frac{1}{3}k_x^2[H^3(\kappa_{(1)} + \eta)] = 0, \tag{4.10}$$

which is formally analogous to the streamwise-invariant dispersion relation derived in Ledda et al. [39], and it can be written in the form $\mathrm{i}\omega\mathbf{I}\eta = \mathbf{L}\eta$. At each streamwise cross-section, the eigenmode is normalized imposing $\int_0^{L_y}\hat{\eta}^H\hat{\eta}\mathrm{d}y = 1$, where $(\cdot)^H$ denotes the transconjugate.

At order $\mathcal{O}(\sigma)$, as detailed in Appendix C of the ESM, a compatibility condition is imposed, resulting in the following amplitude equation:

$$M(X)\frac{\mathrm{d}\mathcal{A}}{\mathrm{d}X} + N(X)\mathcal{A} = 0 \rightarrow \mathcal{A}(X) = \mathcal{A}(0)\exp\left(-\int_0^X \frac{N(X)}{M(X)}\mathrm{d}X'\right). \tag{4.11}$$

The gain is expressed as follows:

$$G^2(\omega, L_x) = \frac{\int_0^{L_x}\mathcal{A}^H\left(x'\right)\mathcal{A}\left(x'\right)\int_0^{L_y}\left(\eta^H\left(x',y\right)\cdot\eta\left(x',y\right)\right)\mathrm{d}y\left(e^{\int_0^{x'}-2\mathrm{Im}(k_x)\mathrm{d}x''}\right)\mathrm{d}x'}{\int_0^{L_y}\eta^H(0,y)\cdot\eta(0,y)\mathrm{d}y}. \tag{4.12}$$

Since at each cross section $\int_0^{L_y}\eta^H\eta\mathrm{d}y = 1$, the total gain simplifies to:

$$G^2(\omega, L_x) = \int_0^{L_x}\mathcal{A}^H\left(x'\right)\mathcal{A}\left(x'\right)\left(e^{\int_0^{x'}-2\mathrm{Im}(k_x)\mathrm{d}x''}\right)\mathrm{d}x'. \tag{4.13}$$

The procedure is as follows. At each streamwise location x, we solve for the dispersion relation (4.10), thus obtaining the streamwise wavenumber and the corresponding eigenvector. Then, the coefficients of equation (4.11) are evaluated and the amplitude is obtained by integration of the ODE.

The baseflow $H(x,y)$ is the steady solution of equation (2.6) outlined in Section 3. The baseflow is then imported in MATLAB for the resolution of the eigenvalue problem (4.10), at each of the considered 500 streamwise locations in the range $0 < x < 225$. No appreciable variations of the results are observed with a larger number of sections along the streamwise

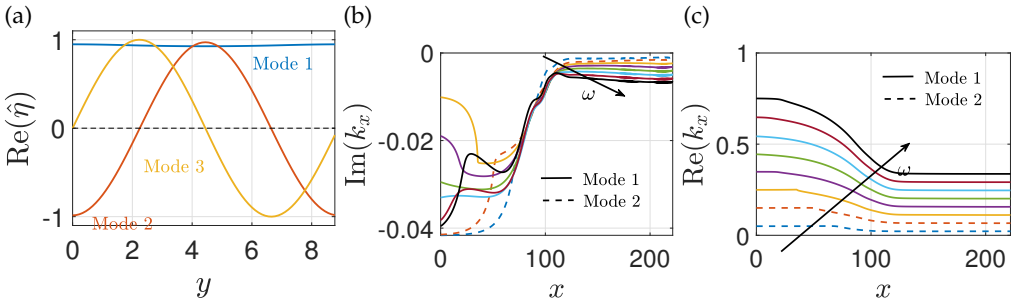

Figure 7: (a) Real part of the three unstable modes at the inlet, for $\omega = 0.5$. (b,c) Imaginary (b) and real (c) parts of the streamwise wavenumber, from the spatial stability analysis, for the downstream unstable mode. The solid and dashed lines respectively denote Modes 1 and 2 at the inlet. The colors identify $\omega = 0.1$ (dashed blue), $\omega = 0.3$ (dashed orange), $\omega = 0.5$ (yellow), $\omega = 0.7$ (purple), $\omega = 0.9$ (green), $\omega = 1.1$ (cyan), $\omega = 1.3$ (maroon), $\omega = 1.5$ (black). The value of the linear advection velocity is $u = 2$.

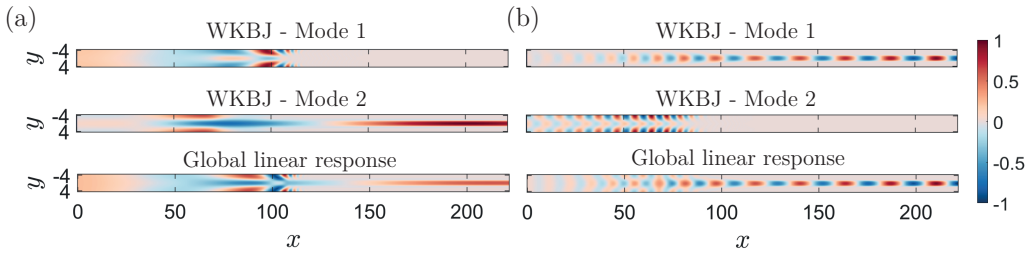

Figure 8: $u = 2$ and (a) $\omega = 0.1$, (b) $\omega = 1.2$. Comparison of the real part of the global linear response (on the bottom) with the WKBJ real part of Mode 1 (top) and Mode 2 (center).

direction. The numerical discretization of the eigenfunction problem is performed using a Fourier pseudospectral collocation method. A preparatory analysis shows that numerical convergence is already achieved with 80 collocation points along the spanwise direction. The adjoint eigenvalue problem, needed for the amplitude equation, is numerically solved by using the discrete adjoint [45]. The derivatives of the baseflow, streamwise wavenumber and eigenvectors, required for the amplitude equation (4.11), are evaluated using second-order finite differences. The numerical integration of equation (4.11) is performed with the built-in MATLAB function *trapz*.

The results of the above-described analysis are now presented. In the context of spatial stability analysis, negative values of the imaginary part of k_x denote unstable configurations associated with downstream propagating waves [19,45,49]. A preliminary analysis at the inlet shows that the spectrum is characterized by three unstable modes associated with downstream propagating waves. The three different modes are tracked along the streamwise direction by using the result in the previous section as the initial guess for the calculation at the successive one. Two of the modes are symmetric with respect to the axis $y = 0$, while the other one is antisymmetric. Figure 7(a) shows the real part of the three modes at the inlet section. We denote as *flat* or *Mode 1* the mode that is almost invariant along the spanwise direction, *cosine* or *Mode 2* the mode analogous to a cosine, and *sine* or *Mode 3* the antisymmetric mode.

We focus on the symmetric modes, while the antisymmetric one is reported in the ESM (Appendix D) as it is not relevant for the dynamics due to the chosen inlet forcing of Section 4(b). For $\omega = 0.1, 0.3$ the unstable lenses mode in the streanwise-invariant rivulet region originates from Mode 2, while for $\omega > 0.5$ it stems from Mode 1 (see figure 7(a)). Figure 7(b,c) shows the streamwise evolution of k_x for different values of the forcing frequency, and $u = 2$. Only the cases

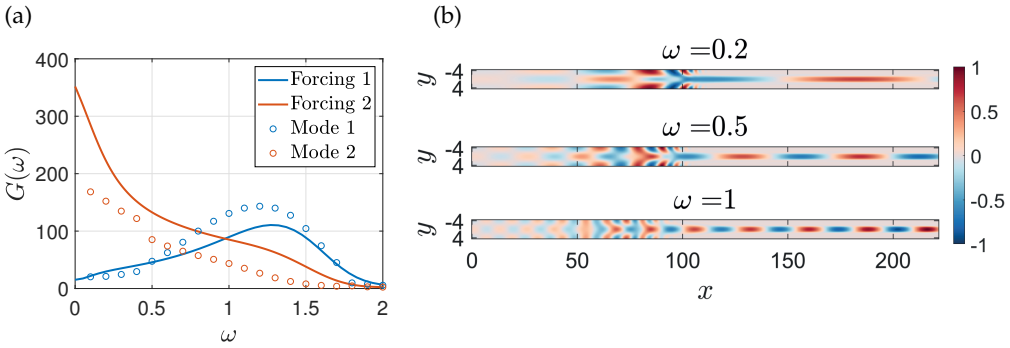

Figure 9: $u = 2$. (a) Gain resulting from the global linear approach, flat (Forcing 1, blue solid line) and cosine (Forcing 2, orange solid line) inlet forcings. The dots are the values of the gain obtained from the WKBJ analysis, flat (Mode 1, blue circles) and cosine (Mode 2, orange circles) inlet modes. (b) Real part of the global linear response with the harmonic cosine forcing at the inlet (Forcing 2). Eigenvectors are rescaled with the maximum absolute value.

that evolve downstream to the unstable mode are reported. The imaginary and real parts of k_x respectively increase and decrease with x, reaching downstream a constant value. An increase of ω, in the considered range, shows a decrease of the real part of k_x.

The amplitude equation (4.11) allows one to connect the different streamwise slices of the modes, whose results for the real part are reported in figure 8, compared to the global linear response of Section 4(b). In panel (a), Mode 1 is amplified until $x \approx 100$, where it presents large values on the sides and is damped downstream. Mode 2 evolves into lenses of extremely large spatial period. In panel (b), Mode 1 survives downstream with smaller lenses, while Mode 2 is damped at $x \approx 100$. The pattern of the global linear response is very similar to the superposition of the modes obtained with the WKBJ approach.

We then move to a quantitative comparison of the gain between the global linear analysis and the WKBJ approach. In figure 9(a), the gain of Modes 1 and 2 are compared with the ones from the global linear analysis with inlet forcing (i) the spanwise-invariant oscillation of the thickness (described in Section 4(b)) (Forcing 1) and (ii) a cosine along the spanwise direction oscillating in time, in analogy to Mode 2 (Forcing 2). The typical linear response to the Forcing 2 is reported in figure 9(b). The gain curve of the Forcing 2 is characterized by a large value of the static gain (i.e. at $\omega = 0$) and $G(\omega)$ decreases with ω. The two gain curves of the global linear response are analogous to those of the WKBJ approach.

The WKBJ analysis reveals that the linear response to harmonic inlet forcing (Section 4(b)) can be interpreted as the superposition of two symmetric modes and only one of these two survives downstream, and is localized in the central lobe of the rivulet. As the rivulet profile saturates, the thickness on the sides is of order 10^{-2}, thus quenching the instability because of the very thin layers of fluid involved in this region. The real part of k_x is decreasing downstream, and thus the perturbation presents larger wavelengths than upstream. This is due to larger advection velocities (proportional to uH^2 [39]) on the central part of the rivulet, compared to regions close to the inlet with lower maximum thickness. The comparison of the global linear analyses with the inlet forcings that reproduce the spatial modes confirms the good agreement in terms of gain and validates the interpretation of the linear response as the interaction of these two modes.

Finally, at very low values of the forcing frequency, the wavelengths of the resulting unstable mode are of the order of the variations of the baseflow, thus violating the hypothesis of slowly-evolving baseflow compared to the perturbation. However, a good agreement is observed also in this case.

In this section, we aimed at interpreting the secondary instability observed in the global linear response of Section 4(b) by a local stability analysis combined with a WKBJ approach.

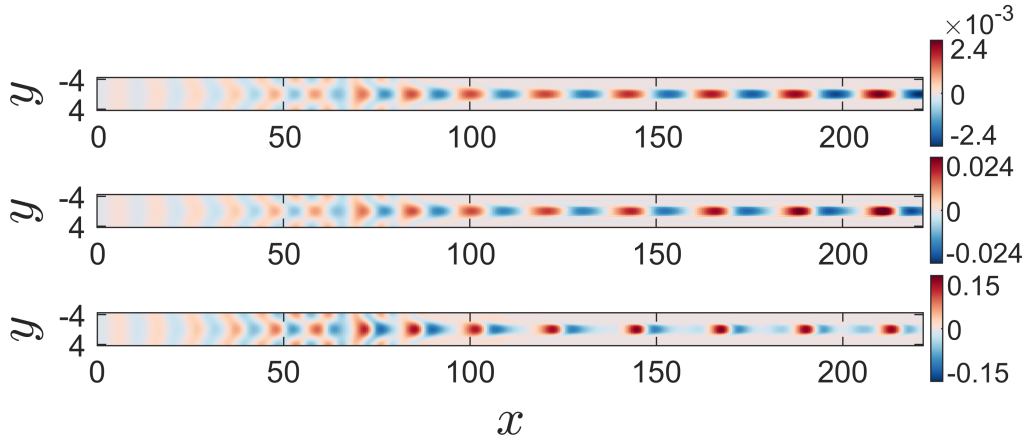

Figure 10: Non-linear response to harmonic forcing at $t = 125$, for $\omega = 1.25$ and $u = 2$, in terms of perturbation $\eta = h - H$. From the top to the bottom: $\varepsilon = 10^{-4}$, $\varepsilon = 10^{-3}$, $\varepsilon = 10^{-2}$.

However, the previous analyses were focused on the linear response. The range of validity of the previous analyses is assessed by investigating the non-linear dynamics. Henceforth, the non-linear response to the inlet forcing described in Section 4(b) is studied.

5. Non-linear response to inlet harmonic forcing

In this section, the non-linear response to harmonic inlet forcing is studied. The non-linear equation (2.6) is thus considered and the evolution of the response with initial condition the steady baseflow $H(x, y)$ described in Section 3 is studied. The Dirichlet boundary condition at the inlet reads:

$$h(x = 0, y, t) = 1 + \mathrm{A}^* \cos(y/\sqrt{2}) + \varepsilon \sin(\omega t), \tag{5.1}$$

where ε and ω are respectively the amplitude and the frequency of the harmonic inlet forcing.

Figure 10 shows the resulting pattern at $t = 125$, for $\omega = 1.25$ and $u = 2$. For $\varepsilon = 10^{-4}$, 10^{-3}, the results show lenses analogous to those of the global linear response, and the amplitude of the response is proportionally increasing with the forcing one. However, already at $\varepsilon = 10^{-2}$, the pattern significantly differs from the previously described linear response, and the amplitude of the response does not follow a linear increase with the forcing amplitude. In figure 11(a) the centerline and side profile for $\varepsilon = 10^{-2}$ is reported. At the centerline, profiles similar to those reported in Kofman et al. [32] and Rohlfs et al. [33] are observed.

As a quantitative comparison with the linear analysis, the non-linear gain is introduced:

$$G^2_{\mathrm{NL}}(\omega, u) = \frac{\overline{\int_\Omega (h - H)^2 \mathrm{d}\Omega}}{\overline{\int_\Gamma (\varepsilon \sin(\omega t))^2 \mathrm{d}\Gamma}}, \tag{5.2}$$

where the overline denotes time averaging. In figure 11(b), the comparison between the non-linear gain and the linear one reveals a very good agreement for $\varepsilon = 10^{-4}$, 10^{-3}. For $\varepsilon = 10^{-2}$ the maximum gain is lower, although the curve resembles the global linear one.

The non-linear simulations confirm the results of the linear analyses when the amplitude of the harmonic forcing is sufficiently small. At larger values of the amplitude of the harmonic forcing, the non-linear effects become predominant and strongly non-linear lenses are observed, with centerline profiles reminiscent of previous analyses [32,33]. A strong saturation mechanism of the amplitudes is observed. In a perspective of flow control, the amplitude of the harmonic inlet forcing thus plays a key role, together with the forcing frequency. For large enough values of

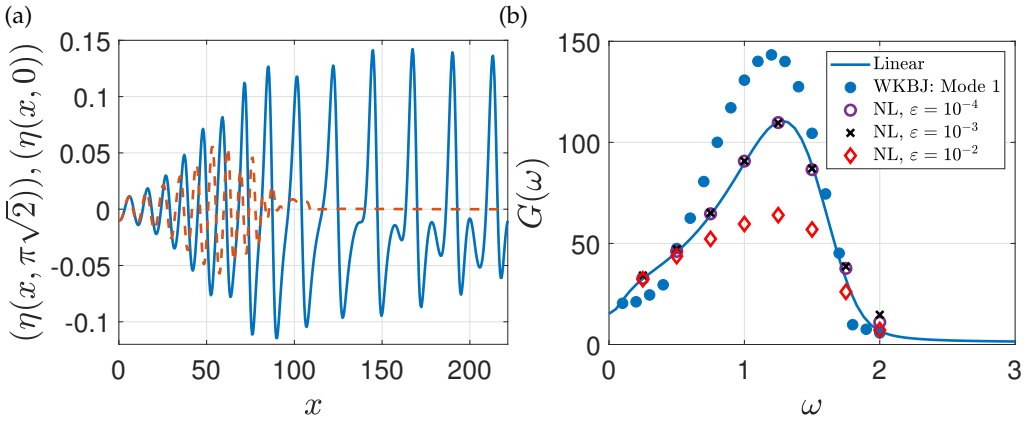

Figure 11: (a) . Perturbation $\eta = h - H$ from the non-linear simulations, at the centerline (solid) and on the lateral boundary (dashed), $\varepsilon = 10^{-2}$, for $u = 2$, $\omega = 1.25$ and $t = 125$. (b) Total gain from the WKBJ approach for Mode 1, the global linear analysis and the non-linear simulations for different values of the inlet amplitude.

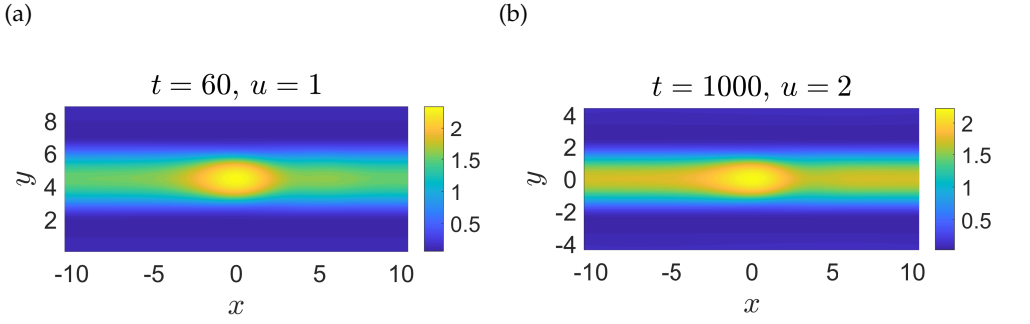

Figure 12: Thickness profile for the non-linear simulation with periodic domain, $k_x = 0.3$. (a) $u = 1$ and $t = 60$, (b) $u = 2$ and $t = 1000$. The x and y scales are the same so as to show the correct aspect ratio of the lens.

the amplitude, a pattern of almost periodic traveling lenses. The amplitude of these lenses slowly evolves downstream when u is sufficiently large.

In this section, the different patterns of lenses emerging from the inlet and the effect of u, frequency and initial amplitude of the harmonic perturbation was characterized. In the following, the late stage of the process of growth and the structure of these lenses in the rivulet region are investigated. Since a parametric study considering the streamwise evolution with inlet and outlet conditions would involve a large number of parameters (ω, u, ε) and require extremely long domains, we first study the evolution of non-linear structures, starting from a rivulet, in a periodic domain of variable streamwise length.

6. Non-linear evolution of traveling lenses in a periodic domain

The present section is devoted to the study of the non-linear evolution of lenses in a periodic domain of respectively streamwise and spanwise size L_p and $L_y = 2\pi\sqrt{2}$. Equation (2.3) is solved with periodic boundary conditions and the following initial condition:

$$h(x, y, 0) = H_r(y) + \varsigma \mathrm{Re}\left(\check{\eta} \exp\left(\mathrm{i}k_x x\right)\right), \quad \varsigma = 10^{-2}. \tag{6.1}$$

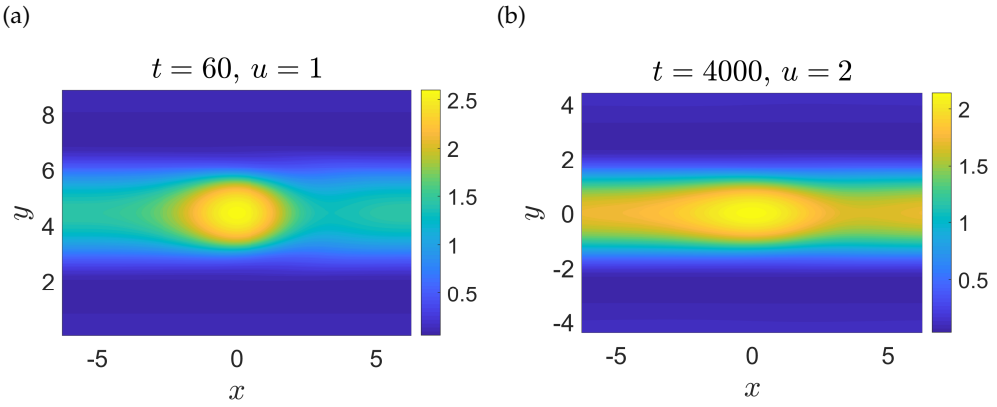

Figure 13: Thickness profile for the non-linear simulation with periodic domain, $k_x = 0.5$. (a) $u = 1$ and $t = 60$, (b) $u = 2$ and $t = 4000$. The x and y scales are the same so as to show the correct aspect ratio of the lens.

$H_r(y)$ is the streamwise-invariant rivulet profile, extended along the streamwise direction, at $t = 400$, obtained from equation (2.3) imposing $\partial_x = 0$, and $\check{\eta}$ is the linear mode obtained from the linear stability analysis of $H_r(y)$ (see Ledda et al. [39] for further detail). The initial condition for the evaluation of $H_r(y)$ is $h = 0.54$, which is the thickness required to have the same flow rate of the simulations with inlet and outlet conditions, in the streamwise-invariant rivulet region [37]. The simulations, in analogy with the previous non-linear ones, are performed in COMSOL Multiphysics.

The influence of u and the streamwise wavenumber of the periodic domain $k_x = 2\pi/L_p$ on the results is now described. Figure 12 shows the thickness profile, at large times, for $k_x = 0.3$ and two different values of u. The large-time solution is characterized by a rivulet carrying a lens, whose profile is similar to an axisymmetric drop. Similar results are obtained increasing u and varying k_x, as in figure 13, which shows a lens traveling on the rivulet, for $k_x = 0.5$. For visualization purposes, the maximum thickness has been repositioned at the center of the domain, since the lens is traveling. In Pier et al. [61], the non-linear response for a fixed k_x gives the non-linear complex dispersion relation between the frequency ω_{NL} and k_x, the streamwise wavenumber itself, for a saturated traveling wave. We extend this idea to the case of a non-saturated response by considering a time-dependent dispersion relation, in which the non-constant and non-linear frequency reads:

$$\omega_{\mathrm{NL}}(t, k_x) = \frac{\mathrm{d}X_{\max}}{\mathrm{d}t} k_x, \tag{6.2}$$

where $X_{\max}$ is the maximum thickness location.

The time evolution shows that the maximum value of the thickness $\max(h)$ always increases as the lens travels (figure 14(a)). A final and rapid blow-up of the solution is always observed, in which the values of the time derivative of the maximum thickness take very large values.

The spatial evolution is deduced by following the maximum value of the thickness that travels in the periodic domain. In figure 14(b) we report the distance L_2 for the blow-up of the solution (dots) and at which $\frac{\mathrm{d}}{\mathrm{d}t} \max(h) > 0.1$ (marked by crosses in figure 14(a)) occurs, as a function of k_x. The distance for the blow-up of the solution strongly increases with u. For $u = 1$ and $u = 1.5$ the behavior of L_2 is non-monotonous with ω, while L_2 increases with ω, for $u = 2$.

The blow-up of the solution is interpreted as the manifestation of the onset of the dripping process, according to Kofman et al. [32] and Indeikina et al. [40]. Both the final simulation distance and the one beyond which $\frac{\mathrm{d}}{\mathrm{d}t} \max(h) > 0.1$ are considered, without appreciable differences. Therefore, a first estimate of the order of magnitude of the dripping distance is given using the results of figure 14.

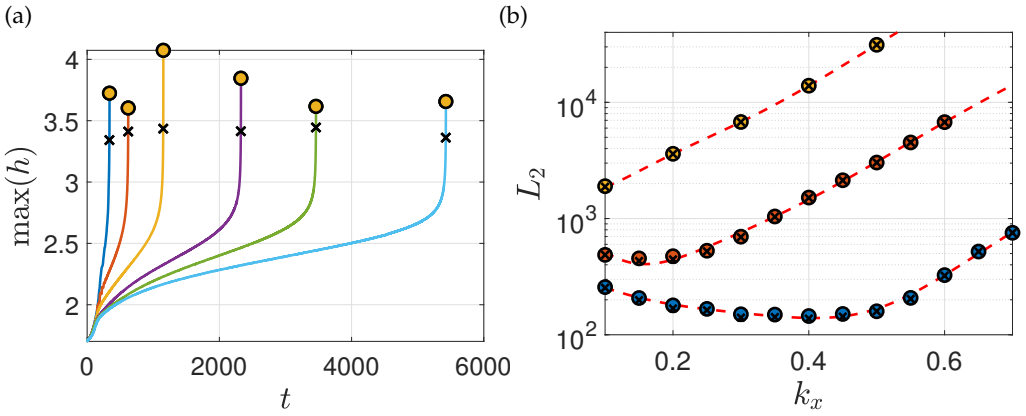

Figure 14: (a) Evolution of the maximum thickness with x for $u=2$, $k_x=0.1$ (blue), $k_x=0.2$ (orange), $k_x=0.3$ (yellow), $k_x=0.4$ (purple), $k_x=0.45$ (green), $k_x=0.5$ (cyan). (b) Distance for the blow-up of the solution (dots) and at which $\frac{\mathrm{d}}{\mathrm{d}t}\max(h)>0.1$ occurs (crosses), for the non-linear simulations in the periodic domain, $u=1$ (blue), $u=1.5$ (orange), $u=2$ (yellow).

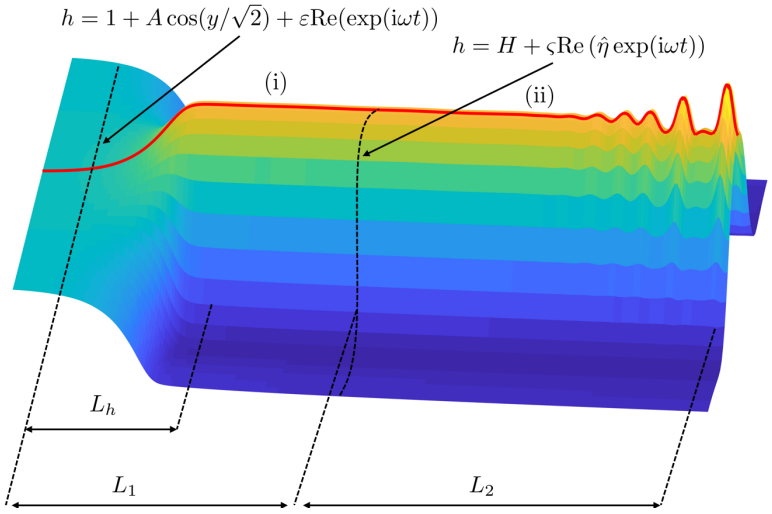

Figure 15: Sketch of the configuration considered for the estimate of the dripping length.

In this section, a first estimate of the order of magnitude of the dripping distance is given. This estimate can be improved considering the streamwise-transient evolution of perturbations at low amplitudes studied in Sections 4(b) and 4(c).

7. An estimate of the dripping length

In the previous section, the non-linear structures emerging from a fully-developed rivulet profile, in a periodic domain of variable streamwise length was studied. However, when inlet and outlet conditions are considered, the growth of perturbations in the region where the rivulet evolves is crucial, as observed in Section 4(b). If the amplitude of the inlet forcing is small enough, the growth of perturbations between the inlet and the saturated rivulet profile follows the linearized dynamics described in Section 4(b). Therefore, in the spirit of Pier [62], the growth of lenses is composed of (i) an initial linear growth described by the linearized dynamics and (ii) by a

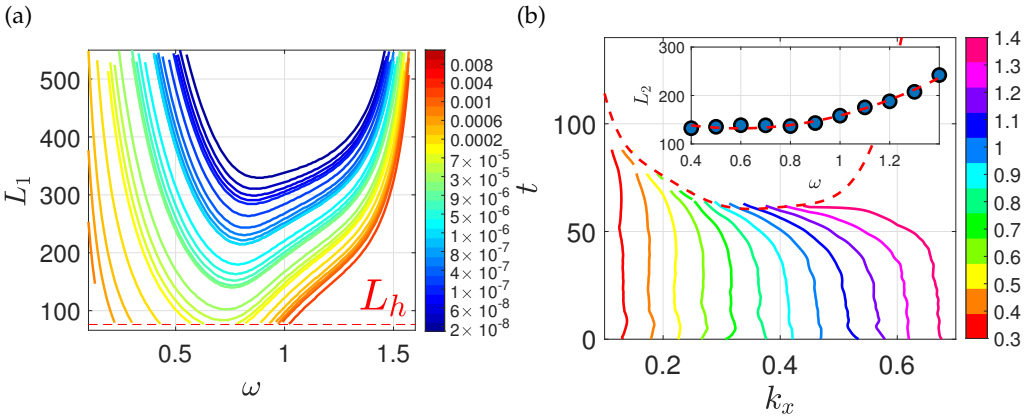

Figure 16: $u = 1$. (a) Variation of L_1 with ω; different colours denote different values of ε according to the colorbar. The red dashed line denotes the healing length L_h. (b) Variation of the non-linear frequency $\omega_{\mathrm{NL}} = \frac{\mathrm{d}X_{\max}}{\mathrm{d}t} k_x$ with time; different colours denote different values of k_x according to the colorbar. The red dashed line denotes the dripping threshold. In the inset: variation of L_2 with ω resulting from the integration in time for fixed ω.

non-linear growth described by the evolution in the periodic domain of the previous section. We consider a harmonic inlet perturbation of frequency ω and amplitude ε, for the steady baseflow $H(x, y)$ described in Section 3, i.e $h(x = 0, y, t) = 1 + \mathrm{A}^* \cos(y/\sqrt{2}) + \varepsilon \mathrm{Re}(\exp(\mathrm{i}\omega t))$.
The transition between stages (i) and (ii) is defined where the maximum value of the thickness perturbation $h - H$ is $\max(h - H) = \varsigma$, where $\varsigma \ll 1$, assumed to be $\varsigma = 10^{-2}$ (see figure 15) according to the simulations of the previous section. In pratice, the distance needed to pass from stage (i) to (ii), identified as $L_1(\omega, \varepsilon, u)$, is obtained from the global linear analysis with inlet and outlet conditions (Section 4(b)) as the coordinate $x = L_1$ at which $\sqrt{L_y}\varepsilon \max(|\eta|) = \varsigma$ (since the inlet condition is given by equation 4.7). In figure 16(a) the variation of L_1 with the forcing frequency ω and for different values of ε, for $u = 1$, is reported. L_1 is non-monotonous with ω, whilst it always decreases with ε.

The dripping distance L_{drip} is thus given by $L_{\mathrm{drip}}(\omega, \varepsilon, u) = L_1(\omega, \varepsilon, u) + L_2(\omega, u)$, where $L_2(\omega, u)$ is obtained from the simulations with double-periodic domain of Section 6 as follows. Since the simulations with inlet and outlet conditions were conducted with an imposed temporal frequency rather than a streamwise spatial forcing, the results of the simulations with periodic domain cannot be directly applied. At each time step, and for each simulation with $k_x = \mathrm{const}$, the instantaneous and non-linear temporal frequency is evaluated using the definition of non-linear phase speed $\omega_{\mathrm{NL}}(t, k_x) = \frac{\mathrm{d}X_{\max}}{\mathrm{d}t} k_x$, where $X_{\max}$ is the maximum thickness location. The results for $u = 1$ is reported in figure 16(b). To evaluate $L_2(\omega, u)$, the iso-contour $\omega_{\mathrm{NL}} = \omega$ is thus followed in time, crossing the values of k_x until we reach the dripping threshold for a time $t = T$. Equation (6.2) is integrated to obtain the dripping distance $L_2(\omega, u)$:

$$L_2 = \int_0^T \frac{\omega}{k_x} \mathrm{d}t. \tag{7.1}$$

The numerical implementation is performed in MATLAB. The non-linear frequency is evaluated with second order finite differences and a time step of $\Delta t = 0.05$, for different k_x whose step is $\Delta k_x = 0.025$. The integral is performed along the iso-level ω_{NL} =const using the built-in MATLAB function *trapz*. The variation of L_2 with ω (for $u = 1$) is reported in the inset of figure 16(b). An increase of L_2 with ω is observed, in the considered parameters range.

Note that the decomposition into L_1 and L_2 only holds if L_1 is larger than the healing length for the fully developed rivulet profile L_h, as the results of Section 6 imply as initial condition a fully developed rivulet and thus cannot be applied, if it has not been attained. Figure 17(a)

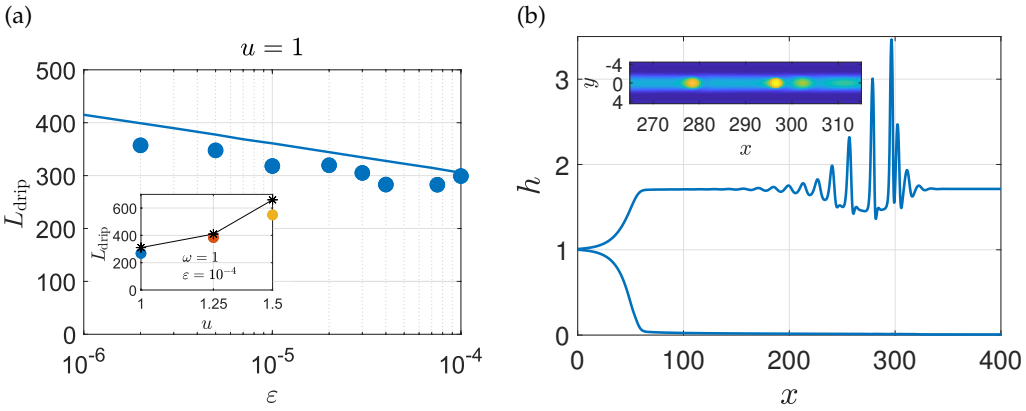

Figure 17: (a) Dripping length $L_{\rm drip}$ as a function of ε, prediction (solid line) and results of the non-linear simulation (dots), for $\omega = 1$ (blue) and $u = 1$. In the inset: dripping length as a function of u, for $\varepsilon = 10^{-4}$ and $\omega = 1$. (b) Maximum and minimum thickness at $t = 150$, for $\varepsilon = 7.5 \times 10^{-5}$ and $\omega = 1$. In the inset: thickness distribution close to the dripping region.

shows the results of the prediction (solid line) compared to the non-linear simulations of equation 2.3 with inlet and outlet conditions (dots) with a domain size of $L_x = 900$, whose thickness distribution at the first dripping onset is reported in panel (b). The non-linear simulation is stopped when the critical value of $\frac{\rm d}{{\rm d}t} \max(h) > 0.1$ is reached for the first time. The prediction fairly agrees with the non-linear simulations results, with a relative error of $\approx 10\%$. The agreement is reasonably good also when u is varied, as reported in the inset of figure 17(a).

In this section, a method to estimate the dripping length by exploiting the results of the global linear analysis and the non-linear simulations in doubly-periodic domain was outlined, for the steady baseflow described in Section 3. As reported in figure 17(b), the non-linear response exhibits non-negligible variations along the streamwise direction at the dripping location, breaking the assumption of traveling and periodic lenses. However, the prediction fairly agrees with the simulations, thus giving a reasonable estimate of the dripping distance as a function of the parameters (ω, ε, u). For the sake of completeness, Appendix E of the ESM shows a generalization of the method when the amplitude of the spanwise sinusoidal perturbation at the inlet is $A < A^*$, i.e. the value assumed to define the reference developing rivulet solution in Section 3. The proposed approach gives a fairly accurate prediction and is suitable for a parametric study, in opposition to the non-linear simulations with inlet and outlet conditions, which do not appear as suitable for describing a complete map of the dripping length in the parameters space.

8. Conclusion and discussion

In this work, the secondary instability of a thin film flowing under an inclined plane when the inlet is temporally forced was studied. Inspired by the experimental results of Lerisson et al. [37], we considered the steady solution of the flow equation, for fixed $\tilde{\ell}_c^* = 1$ and with inlet and outlet conditions, in a spanwise-periodic domain of size $L_y = 2\pi\sqrt{2}$, i.e. the natural spacing of rivulets [37]. The steady baseflow was characterized by a streamwise-invariant state emerging downstream, at a distance found to be linear with u.

The linear response was then studied, with the inlet forced with a harmonic forcing consisting of an oscillation of the thickness around the steady constant value. Thickness perturbations evolved into lenses traveling on the rivulet, whose spacing was found to decrease with the forcing frequency. An increase of the linear advection velocity led to lenses of larger spacing and smaller amplitudes, while the forcing frequency was seen to modify both the spacing and

the amplitude of such lenses. The gain curves showed a maximum, associated with an optimal frequency decreasing with u, which did not vary significantly with the streamwise length of the domain.

The linear response was rationalized via a weakly non-parallel (WKBJ) spatial stability analysis. The linear dynamics was interpreted as the superposition of two linearly unstable modes, one damped and the other one amplified downstream. The gain curves of the linear response were well reproduced by the weakly non-parallel analysis.

For low amplitudes of the forcing, the non-linear response to harmonic forcing showed patterns similar to the linear ones. Associated with an increase of the non-linear effects, lower values of the gain were observed, without relevant changes of the optimal frequency. Trains of almost periodic lenses, slowly evolving downstream, were observed. The non-linear structures were then characterized by studying the evolution in doubly-periodic domains of variable streamwise length, where the blow-up of the solution was interpreted as the initial stage of dripping. A dripping distance was defined by combining the results of the linear response with the non-linear evolution in a doubly-periodic domain, giving an estimate in fair agreement with the non-linear simulations.

Our work provides a description of three-dimensional patterns of a thin film flowing under an inclined plane when the inlet is temporally forced, thus disclosing the existence of regular arrays of traveling lenses on the rivulets. We show the possibility to exploit the flow rate, inclination angle, and the frequency and amplitude of the time-harmonic inlet forcing so as to obtain lenses with different spacings and shapes. These considerations may find further development in manufacturing processes of complex structures by means of curing processes of coatings below surfaces [27]. Besides, we proposed a method to estimate of the dripping distance of a rivulet, both for spatially-periodic structures and when the evolution from the inlet is considered.

This work may be extended in several ways to refine the presented results. First, the case of a rivulet with natural spacing $L_y = 2\pi\sqrt{2}$ was investigated, in which the temporal inlet forcing was small enough so that the dynamics was considered as a perturbation of the steady and spanwise-periodic rivulet. Further developments may include spanwise-periodic rivulets with wavelength differing from the natural one, briefly presented in Lerisson et al. [37]. Another extension is the analysis for different values of $\tilde{\ell}_c^*$ to better characterize the response in the whole parameter space. Last, a lubrication-type approximation to describe the dynamics of lenses was employed. Albeit suitable to describe the first stage of the dripping process, the lubrication model cannot describe the later stages of dripping. Further studies may include the analysis of the process leading to a dripping drop detaching from the rivulet.

Data Accessibility. This article has no additional data.

Competing Interests. We have no competing interests.

Funding. We acknowledge the Swiss National Science Foundation under grant 200021_178971.

References

1. Short MB, Baygents JC, Beck JW, Stone DA, Toomey III RS, Goldstein RE. 2005 Stalactite growth as a free-boundary problem: a geometric law and its platonic ideal. *Physical Review Letters* **94**, 018501.
2. Meakin P, Jamtveit B. 2010 Geological pattern formation by growth and dissolution in aqueous systems. *Proceedings of the Royal Society A: Mathematical, Physical and Engineering Sciences* **466**, 659–694.
3. Camporeale C. 2015 Hydrodynamically locked morphogenesis in karst and ice flutings. *Journal of Fluid Mechanics* **778**, 89–119.
4. Bertagni MB, Camporeale C. 2017 Nonlinear and subharmonic stability analysis in film-driven morphological patterns. *Physical Review E* **96**, 053115.
5. Ledda PG, Balestra G, Lerisson G, Scheid B, Wyart M, Gallaire F. 2021 Hydrodynamic-driven morphogenesis of karst draperies: spatio-temporal analysis of the two-dimensional impulse response. *Journal of Fluid Mechanics* **910**, A53.
6. Weinstein S, Ruschak K. 2004 Coating flows. *Annu. Rev. Fluid Mech.* **36**, 29–53.

7. Lee A, Brun PT, Marthelot J, Balestra G, Gallaire F, Reis PM. 2016 Fabrication of slender elastic shells by the coating of curved surfaces. *Nature Communications* **7**.
8. Kapitza P. 1948 Wave flow of thin layers of viscous liquid. *Zh. Eksper. Teoret. Fiz.* **18**, 3–28.
9. Kapitza P, Kapitza S. 1965 Wave flow of thin layers of a viscous fluid: Experimental study of undulatory flow conditions. *Collected Papers of PL Kapitza (ed. D. Ter Haar)* **2**.
10. Kalliadasis S, Ruyer-Quil C, Scheid B, Velarde M, editors. 2012 *Falling Liquid Films*. Applied Mathematical Sciences. Springer-Verlag London.
11. Oron A. 2000 Nonlinear dynamics of three-dimensional long-wave Marangoni instability in thin liquid films. *Physics of Fluids* **12**, 1633–1645.
12. Hosoi A, Bush JW. 2001 Evaporative instabilities in climbing films. *Journal of fluid Mechanics* **442**, 217.
13. Rubio RG, Ryazantsev YS, Starov VM, Huang GX, Chetverikov AP, Arena P, Nepomnyashchy AA, Ferrus A, Morozov EG. 2013 *Without Bounds: A Scientific Canvas of Nonlinearity and Complex Dynamics*. Springer.
14. Sterman-Cohen E, Oron A. 2020 Dynamics of nonisothermal two-thin-fluid-layer systems subjected to harmonic tangential forcing under Rayleigh–Taylor instability conditions. *Physics of Fluids* **32**, 082113.
15. Huppert HE. 1982 Flow and instability of a viscous current down a slope. *Nature* **300**, 427–429.
16. Spaid M, Homsy G. 1996 Stability of Newtonian and viscoelastic dynamic contact lines. *Physics of Fluids* **8**, 460–478.
17. Lin TS, Kondic L, Filippov A. 2012 Thin films flowing down inverted substrates: Three-dimensional flow. *Physics of Fluids* **24**, 022105.
18. Xue N, Stone HA. 2021 Draining and spreading along geometries that cause converging flows: Viscous gravity currents on a downward-pointing cone and a bowl-shaped hemisphere. *Phys. Rev. Fluids* **6**, 043801.
19. Gallaire F, Brun PT. 2017 Fluid dynamic instabilities: theory and application to pattern forming in complex media. *Philosophical Transactions of the Royal Society A: Mathematical, Physical and Engineering Sciences* **375**, 20160155.
20. Rayleigh. 1882 Investigation of the Character of the Equilibrium of an Incompressible Heavy Fluid of Variable Density. *Proceedings of the London Mathematical Society* **s1-14**, 170–177.
21. Taylor GI. 1950 The instability of liquid surfaces when accelerated in a direction perpendicular to their planes. I. *Proceedings of the Royal Society of London. Series A. Mathematical and Physical Sciences* **201**, 192–196.
22. Chandrasekhar S. 2013 *Hydrodynamic and hydromagnetic stability*. Courier Corporation.
23. Hynes TP. 1978 *Stability of Thin Films.* PhD thesis University of Cambridge.
24. Babchin A, Frenkel A, Levich B, Sivashinsky G. 1983 Nonlinear saturation of Rayleigh–Taylor instability in thin films. *The Physics of fluids* **26**, 3159–3161.
25. Yiantsios SG, Higgins BG. 1989 Rayleigh-Taylor instability in thin viscous films. *Physics of Fluids A: Fluid Dynamics* **1**, 1484–1501.
26. Pitts E. 1974 The stability of pendent liquid drops. Part 2. Axial symmetry. *Journal of Fluid Mechanics* **63**, 487–508.
27. Marthelot J, Strong EF, Reis PM, Brun PT. 2018 Designing soft materials with interfacial instabilities in liquid films. *Nature communications* **9**, 4477.
28. Lister JR, Rallison JM, Rees SJ. 2010 The nonlinear dynamics of pendent drops on a thin film coating the underside of a ceiling. *Journal of Fluid Mechanics* **647**, 239–264.
29. Fermigier M, Limat L, Wesfreid J, Boudinet P, Quilliet C. 1992 Two-dimensional patterns in Rayleigh-Taylor instability of a thin layer. *Journal of Fluid Mechanics* **236**, 349–383.
30. Brun PT, Damiano A, Rieu P, Balestra G, Gallaire F. 2015 Rayleigh-Taylor instability under an inclined plane. *Physics of Fluids* **27**, 084107.
31. Scheid B, Kofman N, Rohlfs W. 2016 Critical inclination for absolute/convective instability transition in inverted falling films. *Physics of Fluids* **28**, 044107.
32. Kofman N, Rohlfs W, Gallaire F, Scheid B, Ruyer-Quil C. 2018 Prediction of two-dimensional dripping onset of a liquid film under an inclined plane. *International Journal of Multiphase Flow* **104**, 286–293.
33. Rohlfs W, Pischke P, Scheid B. 2017 Hydrodynamic waves in films flowing under an inclined plane. *Physical Review Fluids* **2**, 044003.
34. Charogiannis A, Denner F, van Wachem BGM, Kalliadasis S, Scheid B, Markides CN. 2018 Experimental investigations of liquid falling films flowing under an inclined planar substrate. *Physical Review Fluids* **3**, 114002.

35. Lerisson G, Ledda PG, Balestra G, Gallaire F. 2019 Dripping down the rivulet. *Phys. Rev. Fluids* **4**, 100504.
36. Rietz M, Scheid B, Gallaire F, Kofman N, Kneer R, Rohlfs W. 2017 Dynamics of falling films on the outside of a vertical rotating cylinder: waves, rivulets and dripping transitions. *Journal of Fluid Mechanics* **832**, 189–211.
37. Lerisson G, Ledda PG, Balestra G, Gallaire F. 2020 Instability of a thin viscous film flowing under an inclined substrate: steady patterns. *Journal of Fluid Mechanics* **898**, A6.
38. Pitts E. 1973 The stability of pendent liquid drops. Part 1. Drops formed in a narrow gap. *Journal of Fluid Mechanics* **59**, 753–767.
39. Ledda PG, Lerisson G, Balestra G, Gallaire F. 2020 Instability of a thin viscous film flowing under an inclined substrate: the emergence and stability of rivulets. *Journal of Fluid Mechanics* **904**, A23.
40. Indeikina A, Veretennikov I, Chang HC. 1997 Drop fall-off from pendent rivulets. *Journal of Fluid Mechanics* **338**, 173–201.
41. Garnaud X, Lesshafft L, Schmid P, Huerre P. 2013 The preferred mode of incompressible jets: linear frequency response analysis. *Journal of Fluid Mechanics* **716**, 189–202.
42. Boujo E, Ehrenstein U, Gallaire F. 2013 Open-loop control of noise amplification in a separated boundary layer flow. *Physics of Fluids* **25**, 124106.
43. Boujo E, Gallaire F. 2015 Sensitivity and open-loop control of stochastic response in a noise amplifier flow: the backward-facing step. *Journal of Fluid Mechanics* **762**, 361–392.
44. Shukla I, Gallaire F. 2020 Frequency selection in a gravitationally stretched capillary jet in the jetting regime. *Journal of Fluid Mechanics* **894**, A6.
45. Schmid PJ, Henningson DS, Jankowski D. 2002 Stability and transition in shear flows. Applied mathematical sciences, Vol. 142. *Appl. Mech. Rev.* **55**, B57–B59.
46. Chomaz JM. 2005 Global instabilities in spatially developing flows: Non-Normality and Nonlinearity. *Annual Review of Fluid Mechanics* **37**, 357–392.
47. Theofilis V. 2011 Global Linear Instability. *Annual Review of Fluid Mechanics* **43**, 319–352.
48. Gaster M, Kit E, Wygnanski I. 1985 Large-scale structures in a forced turbulent mixing layer. *Journal of Fluid Mechanics* **150**, 23–39.
49. Huerre P, Rossi M. 1998 p. 81–294. In *Hydrodynamic instabilities in open flows*, Collection Alea-Saclay: Monographs and Texts in Statistical Physics p. 81–294. Cambridge University Press.
50. Chang H. 1994 Wave evolution on a falling film. *Annual review of fluid mechanics* **26**, 103–136.
51. Benney DJ. 1966 Long Waves on Liquid Films. *Journal of Mathematics and Physics* **45**, 150–155.
52. Oron A, Davis SH, Bankoff SG. 1997 Long-scale evolution of thin liquid films. *Reviews of modern physics* **69**, 931.
53. Scheid B, Ruyer-Quil C, Thiele U, Kabov OA, Legros JC, Colinet P. 2005 Validity domain of the Benney equation including the Marangoni effect for closed and open flows. *Journal of Fluid Mechanics* **527**, 303–335.
54. Pumir A, Manneville P, Pomeau Y. 1983 On solitary waves running down an inclined plane. *Journal of fluid mechanics* **135**, 27–50.
55. Ruyer-Quil C, Manneville P. 2000 Improved modeling of flows down inclined planes. *The European Physical Journal B-Condensed Matter and Complex Systems* **15**, 357–369.
56. Ruschak K. 1978 Flow of a falling film into a pool. *AIChE Journal* **24**, 705–709.
57. Wilson SD. 1982 The drag-out problem in film coating theory. *Journal of Engineering Mathematics* **16**, 209–221.
58. Kheshgi H, Kistler S, Scriven L. 1992 Rising and falling film flows: viewed from a first-order approximation. *Chemical engineering science* **47**, 683–694.
59. Högberg M, Henningson D. 1998 Secondary instability of cross-flow vortices in Falkner–Skan–Cooke boundary layers. *Journal of Fluid Mechanics* **368**, 339–357.
60. Viola F, Arratia C, Gallaire F. 2016 Mode selection in trailing vortices: harmonic response of the non-parallel Batchelor vortex. *Journal of Fluid Mechanics* **790**, 523–552.
61. Pier B, Huerre P, Chomaz JM. 2001 Bifurcation to fully nonlinear synchronized structures in slowly varying media. *Physica D: Nonlinear Phenomena* **148**, 49–96.
62. Pier B. 2003 Open-loop control of absolutely unstable domains. *Proceedings of the Royal Society of London. Series A: Mathematical, Physical and Engineering Sciences* **459**, 1105–1115.

View publication stats